PHYSICAL REVIEW FLUIDS **5**, 104603 (2020)

Phase transitions and flux-loop metastable states in rotating turbulence

P. Clark Di Leoni,[1] A. Alexakis,[2] L. Biferale,[3] and M. Buzzicotti[3]
[1]*Department of Mechanical Engineering, Johns Hopkins University, Baltimore, Maryland 21218, USA*
[2]*Laboratoire de Physique de l'École Normale Supérieure, CNRS, PSL Research University, Sorbonne Université, Université de Paris, F-75005 Paris, France*
[3]*Department of Physics and INFN, University of Rome "Tor Vergata," Rome 00133, Italy*

(Received 18 February 2020; accepted 23 September 2020;
published 12 October 2020)

By using direct numerical simulations of up to a resolution of $512 \times 512 \times 32\,768$ grid points we discover the existence of a metastable out-of-equilibrium state in rotating turbulence. We scan the phase space by varying both the rotation rate (proportional to the inverse of the Rossby number, Ro) and the dimensionless aspect ratio, $\lambda = H/L$, where L and H are the sizes of the domain perpendicular and parallel to the direction of rotation, respectively. We show the existence of three turbulent phases. For small Ro but finite λ, we have a split cascade where the injected energy is transferred to both large and small scales. For large λ and finite Ro there is no inverse cascade and the energy is transferred downscale in Fourier space only. Surprisingly, between these two regimes, a third phase is observed as reported here. Consequently, for certain intervals of Ro and λ, energy is no longer accumulated at arbitrarily large scales; rather, it stops at some characteristic intermediate length scales from where it is then redistributed forward in Fourier space, leading to a flux-loop mechanism where the flow is out of equilibrium with vanishing net flux and nonvanishing heterochiral and homochiral subfluxes. The system is further characterized by the presence of metastability explaining why previous numerical simulations were not able to detect this phenomenon, requiring an extremely long observation time and huge computational resources.

DOI: 10.1103/PhysRevFluids.5.104603

I. INTRODUCTION

Statistical systems can develop critical behavior, with abrupt macroscopic changes at varying some control parameters, like temperature or magnetic field [1]. Averaged quantities can show discontinuous or continuous variations across the critical lines/points where the transition occurs in the phase space. Experimental and numerical realizations can be affected by long transients generated by the presence of metastable states corresponding to local minima of the (free) energy [2,3]. Many attempts have tried to transfer such descriptions to out-of-equilibrium systems quantitatively [4,5]. The critical behavior of stationary systems in the presence of energy injection mechanisms, dissipation, and nonvanishing fluxes remains a major topic of current research in fluid dynamics and granular and active matter and lacks systematic theoretical understanding [6–8]. A paradigmatic example of a (phase) transition is the laminar/turbulent jump observed in Poiseuille and Couette flows when changing the forcing intensity [9–11]. In this paper, we investigate the important case of rotating turbulence where the control parameter, given by the intensity of the Coriolis force, affects the symmetries of the macroscopic flow without injecting energy [12–16]. In this setup, it is known that for sufficiently weak rotation rate, Ω, the system behaves as 3D homogeneous and isotropic turbulence transferring energy to small scales only (*forward energy cascade*), while for Ω above a critical value, Ω_c, 3D fluctuations are suppressed, the flow becomes quasi-2D, and energy is transferred with a *split cascade* to large scales also [7,17]. As the domain size H in the direction of rotation becomes larger, Ω_c increases [18–20]. Arguments based on wave-turbulence theory suggest that the inverse flux vanishes in the infinite volume limit, predicting that $\lim_{H\to\infty}\Omega_c \to \infty$ [21]. More recently, considering an asymptotic form of the governing equations for large Ω, it was shown that $\Omega_c \propto H$ [22]. However, for finite Ω we do not know the precise functional dependence of the boundary $\Omega_c(H)$ or the nature of the transition. Despite the importance of such questions for many geophysical and engineering applications we still do not have a satisfying understanding of any of them. In this paper, we report about an even richer phenomenology due to the existence of a region in the (λ, Ro) phase space, where turbulence develops a third macroscopic out-of-equilibrium metastable state, characterized by a *flux-loop cascade*, where the flow organizes to spontaneously stop the tendency to condensate energy in larger and larger scales and enters a stationary regime characterized by the presence of a quasiordered array of turbulent columnar vortices, akin to a vortex crystal [23].

II. PHYSICAL AND NUMERICAL SETUP

We begin by considering the flow in a rectangular periodic domain with aspect ratio $\lambda \equiv H/L$ and dimensions $2\pi L \times 2\pi L \times 2\pi H$ in a rotating frame where rotation is along the direction with dimension $2\pi H$. The governing equations for the incompressible velocity field, $\mathbf{u}$, are

$$\partial_t \mathbf{u} + \mathbf{u}\cdot\nabla\mathbf{u} + 2\boldsymbol{\Omega}\times\mathbf{u} = -\nabla P + \nu\Delta\mathbf{u} + \mathbf{f}, \tag{1}$$

where ν is the kinematic viscosity, $\mathbf{f}$ is an external forcing, and $2\boldsymbol{\Omega}\times\mathbf{u}$ is the Coriolis force produced by the frame rotating with intensity Ω. The forcing term $\mathbf{f}$ used is divergence free and is a delta-correlated random process, which in Fourier space can be written as

$$\langle \hat{\boldsymbol{f}}(t,\boldsymbol{k})\hat{\boldsymbol{f}}^{*}(t',\boldsymbol{q})\rangle = f_0\Theta(k_f)\delta_{k,q}\delta(t-t'), \tag{2}$$

where $\Theta(k_f)$ is a stepwise function that is equal to one between the modes with amplitude k_f and k_f+2. The amplitude chosen was $f_0 = f_1/\lambda$ (see Table I for values), so that the total injection rate $\epsilon = \langle \boldsymbol{f}\cdot\boldsymbol{u}\rangle$ remains fixed, where $\langle\bullet\rangle$ means an average over the forcing realization or on the whole fluid volume. In order to reduce viscous effects and be able to push the inertial range and thus have a wide enough range for the inverse cascades but at the expense of generating bottlenecks at high wave numbers [24], we used a hyperviscosity model where the momentum equations takes the form

$$\partial_t \boldsymbol{u} + \boldsymbol{u}\cdot\nabla\boldsymbol{u} + 2\boldsymbol{\Omega}\times\boldsymbol{u} = -\nabla p + \nu(-1)^{\alpha+1}\Delta^{\alpha}\boldsymbol{u} + \boldsymbol{f} \tag{3}$$

with $\alpha = 2$.

In the present work, we keep $k_f L = 20$ fixed (except when explicitly noted), using λ as control parameter. Besides λ the other two nondimensional quantities are given by Rossby, $\mathrm{Ro} = \epsilon^{1/3}k_f^{2/3}\Omega^{-1}$, and Reynolds, $\mathrm{Re} = \epsilon^{1/3}k_f^{-4/3}\nu^{-1}$, numbers. Time-evolving quantities are shown as a function of $\tilde{t} = t/\tau_f$ where $\tau_f = (\epsilon k_f^2)^{-1/3}$ is the characteristic time associated with the forcing. The equations are solved using a parallel pseudospectral code (see details in Ref. [25]) using grids as big as $512 \times 512 \times 32\,768$ for the largest aspect ratio $\lambda = 64$. It is important to stress that accessing high aspect ratios is key to attack the *infinite volume* limit in the direction parallel to rotation and to assess potential singular effects induced by a finite separation of the 2D plane at $k_\parallel = 0$ from the 3D modes with $k_\parallel > 0$ in Fourier space [26]. We also fixed $L = 1$ and $\epsilon = 1$. In Table I we provide a list of all parameters used in each of the simulations presented in this paper.

III. RESULTS

A. Identification and characterization of macroscopical states

Figure 1(a) summarizes the main results of our paper, showing the existence of three different macroscopic *phases* of the rotating flow in the (λ, Ro) space, consisting of (1) a pure forward-cascade regime, (2) a new flux-loop regime (the choice of name will become obvious later),

TABLE I. All simulations were produced with a horizontal resolution of $N_x = N_y = 512$, box size $L = 2\pi$, hyperviscosity of order $\alpha = 2$, forcing wave number in the range range $[k_f, k_f + 2]$ with $k_f = 20$, forcing amplitude $f_0 = f_1/\lambda$ with $f_1 = 1.66$, viscosity $\nu = 4 \times 10^{-7}$, energy injection rate of $\epsilon = 2.02$, and Reynolds number defined on the forcing scale Re = 125 (see main text). The parameters shown in the table are the box aspect ratio $\lambda = H/L$, the number of collocation points in the vertical direction N_z, rotation rate Ω, Rossby number defined in terms of the energy injection properties, $\mathrm{Ro} = (\varepsilon_f k_f^2)^{1/3}/\Omega$, and the regime the simulation is in.

λ	N_z	Ω	Ro	Regime	t_f/τ_f
1	512	37.5	0.204	Split	764
1	512	34	0.225	Split	601
1	512	33	0.232	Split	373
1	512	30	0.255	Split	1041
1	512	26	0.294	Split	565
1	512	22.5	0.340	Split	938
1	512	20	0.382	Split	469
1	512	18.75	0.408	Split	1480
1	512	17	0.450	Flux loop	649
1	512	15	0.510	Flux loop	1065
1	512	15	0.501	Flux loop	9418
1	512	13.5	0.566	Flux loop	1161
1	512	12.5	0.611	Flux loop	2997
1	512	11.6	0.659	Forward	1215
1	512	10.8	0.708	Forward	1203
1	512	10	0.764	Forward	1480
1	512	7.5	1.019	Forward	3249
2	1024	40	0.191	Split	229
2	1024	32	0.239	Split	470
2	1024	30	0.242	Split	1380
2	1024	28	0.274	Split	1088
2	1024	15	0.481	Split	1887
2	1024	27.5	0.278	Flux loop	657
2	1024	26.4	0.290	Flux loop	615
2	1024	22.5	0.340	Flux loop	663
2	1024	18	0.425	Flux loop	747
2	1024	16.5	0.464	Flux loop	657
2	1024	14.5	0.528	Flux loop	440
2	1024	13.9	0.551	Flux loop	1760
2	1024	12.5	0.613	Forward	1025
4	2048	70	0.109	Split	663
4	2048	60	0.128	Split	871
4	2048	50	0.153	Flux loop	778
4	2048	42.5	0.180	Flux loop	1019
4	2048	30	0.249	Flux loop	2298
4	2048	27.5	0.279	Flux loop	856
4	2048	20	0.383	Flux loop	1049
4	2048	15	0.507	Flux loop	6398
4	2048	13.9	0.551	Forward	1749
4	2048	12.5	0.613	Forward	1116
8	4096	30	0.246	Flux loop	1519
16	8192	30	0.246	Flux loop	1296
32	16384	30	0.244	Flux loop	1136
64	32768	30	0.247	Flux loop	988

TABLE I. *(Continued.)*

λ	N_z	Ω	Ro	Regime	t_f/τ_f
8	4096	15	0.511	Forward	3510
16	8192	15	0.480	Forward	1531
32	16384	15	0.481	Forward	1507
64	32768	15	0.479	Forward	1181

and (3) a split-cascade regime. In Fig. 1(b) we show for the subset of simulations with $\lambda = 1$ and at various Ro the isotropic energy spectra, defined as

$$E_k(t) = \frac{1}{2} \sum_{k \leqslant |\boldsymbol{k}| < k+1} |\hat{\boldsymbol{u}}_{\boldsymbol{k}}(t)|^2,$$

where $\hat{\boldsymbol{u}}_{\boldsymbol{k}}(t)$ are the Fourier coefficients of the velocity field, evaluated at the end of each respective simulation. The direct cascade regime (black dashed lines) does not develop any large-scale fluctuations and peaks at the forcing scale. The split-cascade regime (blue dash-dotted curves) showcases both forward and inverse cascades, and the simulations are stopped when the peak at the largest horizontal scale, $k \simeq 1$, is well developed. The novelty here is given by the flux-loop phase (solid green lines) showing an intermediate spectral behavior. In this case, the energy spectra are much more irregular, break self-similarity, and have their largest peak at an intermediate wave number, $k \simeq 5$. To emphasize this the inset of Fig. 1(b) shows the evolution for the integral length $(\ell/L)^{-1}(\tilde{t}) = L \int kE(k,\tilde{t})\,dk / \int E(k,\tilde{t})\,dk$. It tends to three distinct values depending on the case: the full box size L for the split-cascade case, an intermediate value $\ell \sim L/5$ for the flux loop, and $\ell \sim 1/k_f$ for the forward cascade. Finally Fig. 1(c) shows the evolution of the total energy, $E(\tilde{t}) = \sum_k E_k(\tilde{t})$, for some of the most characteristic (λ, Ro) values. The energy in the forward cascade saturates quickly to a small value. In the split-cascade regime, the energy increases constantly. For the flux-loop cases, all curves change concavity approaching saturation at times well before any sign of saturation is observed for the split-cascade case.

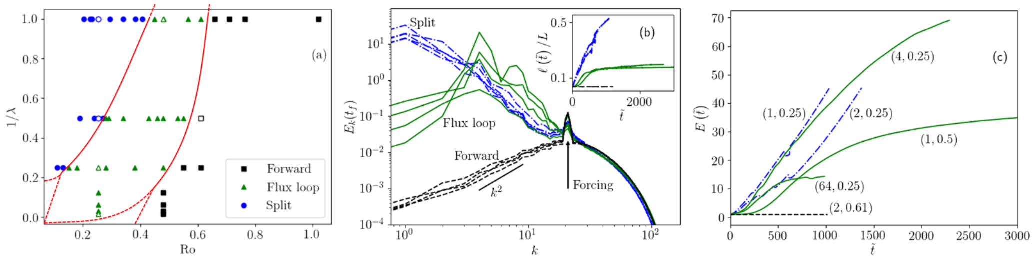

FIG. 1. (a) (λ, Ro) Phase space. Different symbols represent the three macroscopic turbulent cascade phases: forward, flux loop, and split. Red continuous lines are a guide for the eye to distinguish the three phases. Red dotted lines represents possible asymptotics behavior in the limit $\text{Ro} \to 0$ and $\lambda \to \infty$ (see discussion in the text). The time evolution of the energy of the simulations marked with empty symbols is shown in panel (c). (b) Instantaneous energy spectra for fixed aspect ratio, $\lambda = 1$, at different Rossby numbers $0.1 \leqslant \text{Ro} \leqslant 1$. For flux-loop and direct cascade cases the spectra are plotted in the stationary regime; for the split-cascade regime we used the final time when we stopped the simulation. All spectra are evaluated at t_f, the final time of each respective simulation. Inset: time evolution of the integral scale $\ell(\tilde{t})/L$ for some of the simulations. (c) Time evolution of the total energy, $E(\tilde{t})$, for some characteristic (λ, Ro) values [represented with empty symbols in panel (a)]. Line colors distinguish the three phases following the same color code of symbols in panel (a).

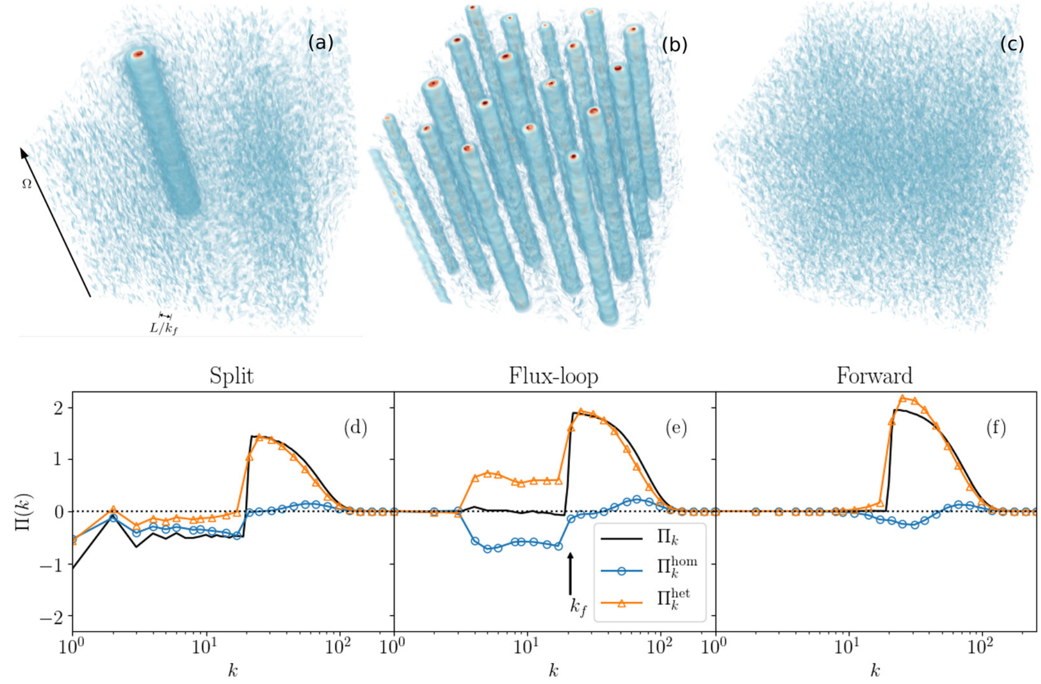

FIG. 2. (a–c) Visualizations of the parallel component of the vorticity for a split-cascade case, a flux loop case, and a forward-cascade case, respectively. The direction of the rotation axis and the forcing length are shown in (a). The three simulations have $\lambda = 1$ and $\mathrm{Ro} = 0.25$, 0.50, and 0.71, respectively. (d–f) Total and chirally decomposed fluxes, for the three regimes shown in the top row.

In Figs. 2(a)–(c) we show visualizations of the vorticity projection in the direction of the rotation axis for three characteristic data sets representing the three different phases at late times, and in the Supplemental Material we show movies comparing their time evolutions (see Appendix B and Ref. [27]). In the split-cascade regime [Fig. 2(a)], the system forms many corotating columnar vortices which eventually merge into one. In the forward-cascade regime [Fig. 2(c)], no large-scale coherent vortical structures are formed, as expected. In the new flux-loop regime [Fig. 2(b)], the columnar vortices form but do not merge and get quasistuck in a lattice-like structure that persists in time (the movie in the Supplemental Material [27] shows this explicitly). Similar structures, deemed "vortex crystals," have been observed in systems like 2D point vortices [23,28], 2D turbulence [29–31], Bose-Einstein condensates [32,33], and even Jupiter's atmosphere [34]. In particular, asymmetric states where the system resembles a crystal with defects, like what is shown in Fig. 2(b), have been shown to be equilibria of corotating point vortex systems [23,28]. Note that in 2D randomly forced turbulence there is a symmetry between positive and negative vorticity. As a result, the kind of structures that we observe here are connected to the asymmetry between corotating and counterrotating vortices introduced by rotation and 3D effects.

It is worth noting that the vortex crystal state is formed in the absence of any large-scale damping term to suppress the inverse cascade. The stationarity of the energy spectrum then implies that the total inverse energy flux at $k < k_f$ has to be zero. Nonetheless, the spectrum is far from the $E_k \propto k^2$ shape predicted by a simple equilibrium distribution [35,36]. To resolve this puzzle we show in Figs. 2(d)–(f) the total energy flux, $\Pi_k = -i \sum_{|\boldsymbol{k}|\leqslant k} \sum_{\boldsymbol{p}+\boldsymbol{q}=\boldsymbol{k}} (\hat{\boldsymbol{u}}_{-\boldsymbol{k}} \cdot \hat{\boldsymbol{u}}_{\boldsymbol{p}})(\boldsymbol{k} \cdot \hat{\boldsymbol{u}}_{\boldsymbol{q}})$, and its exact decomposition in homochiral and heterochiral subcomponents, $\Pi_k = \Pi_k^{\rm hom} + \Pi_k^{\rm het}$, built in terms of Fourier triads including modes with the same or opposite helicity signatures (see Appendix A and Refs. [26,37] for a discussion about the importance of hetero- and homochiral properties for

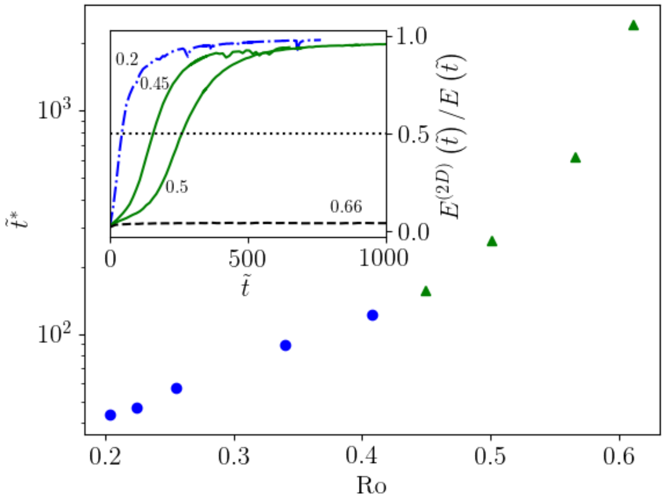

FIG. 3. Time to bidimensionalization t^* as a function of Rossby number for aspect ratio $\lambda = 1$. Inset: Ratio of the energy in the quasi-2D modes a function of time.

the energy cascade direction). In order to reduce fluctuations, fluxes are averaged on stationary or quasistationary time windows. As one can see, the forward cascade [Fig. 2(f)] does not show any exotic behavior; both the total flux and its subcomponents are zero in the $k < k_f$ range [38,39]. For the split-cascade phase in the range $k < k_f$ [Fig. 2(d)] we have the usual negative total flux as a result of the negative contributions from the two helical subcomponents (in a quasi-2D regime helicity does not play any role, and homo- and heterochiral channels are expected to be identical [40,41]). The interesting and nontrivial result is shown in Fig. 2(e), where the total flux for $k < k_f$ is zero, as it must be if the statistics are stationary, but it is the result of a balance between the forward, $\Pi_k^{\text{het}} > 0$, and the inverse, $\Pi_k^{\text{hom}} < 0$, subflux contributions. Hence the name of a flux-loop state [7]. This highly intricate flux-loop balance is an out-of-equilibrium effect and has already been observed in 2D but three-component flows [40] and in rotating flows with only three-component motions [42] where similar peaked spectra were found.

From previous figures it is clear that the inverse cascade and the flux-loop phase are the results of a competition between a tendency to become 2D-like contrasted by some residual 3D structures that push energy forward. It is therefore interesting to assess the dynamical effects of these contrasting forces. To do that, we measured the typical time it takes the energy to become concentrated near the $k_\parallel \approx 0$ plane, defined as the instant of time, t^*, when the ratio $E^{(2D)}(t^*)/E(t^*)$ becomes 0.5, where $E^{(2D)}(t) = \sum_{|\boldsymbol{k}\cdot\boldsymbol{\Omega}|<1} \frac{1}{2}|\hat{\boldsymbol{u}}_{\boldsymbol{k}}|^2$ is the energy in quasi-2D modes. In the inset of Fig. 3 we show the evolution of $E^{(2D)}(\tilde{t})/E(\tilde{t})$ as a function of time for four different values of Ro. For both the split and the flux-loop cases the flow asymptotically approaches quasi-2D states. The main panel of Fig. 3 shows the time $\tilde{t}^*$ versus Ro in a log-linear plot at fixed λ. When entering the flux-loop region, $\tilde{t}^*$ becomes extremely large and increases with Ro faster than exponentially, indicating the presence of a possible divergence at the critical value of $\text{Ro}_c \simeq 0.65$. The transition from the split to the forward cascade as a function of the Rossby number has been also analyzed in a recent important study [20], but with runs that evolved until $t^* = 30$ only, and thus miss the development of the flux-loop regime. In fact, the critical Rossby number reported in Ref. [20] is around the same value where we see the transition from split to flux-loop cascades, and the growth rates they report (measured by the rate of change of the vertical correlations) depend exponentially on Ro, the same way $\tilde{t}^*$ does for $\text{Ro} < 0.4$. We note that $\tilde{t}^*$ indicates the time that the system becomes quasi-2D and starts to transfer energy inversely that is well before the split or the flux-loop state is fully developed. For this reason $\tilde{t}^*$ shows a smooth transition between these two states and diverges only when the forward-cascade regime is approached. Different observables, based, for example, on the integral length, are more suitable to distinguish the properties of the split and flux-loop cascade.

B. Metastability

An important characteristic of the vortex crystals formed in the flux-loop regime is that they are metastable, in the sense that the flow is trapped in this state for very long times (but can escape due to fluctuations) and its appearance depends on the initial conditions and forcing history. Both of these properties have been checked explicitly. The first one was checked by taking a stable simulation under the flux-loop regime and sufficiently decreasing Ro. We found that this action destabilized the vortex-crystal, forced the columns to merge, and made the system switch to the split-cascade regime. However, the opposite is not true. When Ro is increased back to its initial value the system does not return to the crystal state.

The second characteristic was checked by analyzing simulations with the same parameters but different initial conditions and forcing history. We found that some simulations were able to stabilize around a vortex crystal state, while others could not. In Fig. 4 we show an example coming from two simulations performed with the same parameters $(1, 0.45)$ but starting with different initial conditions. In Fig. 4(a) we show the evolution of the total energy along with the visualizations of the parallel component of the vorticity at different times in the insets, and in Fig. 4(b) we show the energy spectra corresponding to both simulations, with the evolution of the integral scale also shown in the inset. The simulation denoted with a solid green line forms a stable vortex crystal and gets stuck in the flux-loop phase. The simulation denoted with blue line and round markers forms a vortex crystal for a short time but then becomes unstable and switches to a dual-cascade regime. Similarly as to what happens in the movie in the Supplemental Material [27], the vortices present in the simulation start to merge when the system transitions to the split-cascade regime. We note that the energy in the simulation entering the flux-loop regime has not yet saturated, nonetheless as its integral scale has saturated and the peaks in its spectra are stable we can assess that the simulation has reached the flux-loop state.

C. Robustness with respect to box size and Reynolds numbers

We present three figures showcasing the robustness of the flux-loop state when changing box size and Reynolds number. In Fig. 5(a) we show the energy spectra for two simulations with $\lambda = 1$ and $\mathrm{Ro} = 0.5$, but different Reynolds numbers. The simulation denoted with the solid line was performed with all the parameters as Table I, while the simulation denoted with the dashed line was performed using twice the linear resolution in every direction, so $N_x = N_y = N_z = 1024$ and with a viscosity of 8×10^{-8}. The inset shows the evolution of their respective integral lengths. The flux-loop state, characterized by a peak spectra and small value of the integral length, is achieved for both cases. In Fig. 5(b) we show the energy spectra for two simulations with $\lambda = 16$ and $\mathrm{Ro} = 0.25$, but different Reynolds number too. Here the difference in the Reynolds number stems from the simulations being forced at a different wave number, where data shown with a dashed line are forced at $k_f = 9$, instead of $k_f = 20$ as in all other simulations. The inset shows the evolution of their respective integral lengths. Again, the flux loop is sustained even when changing the forcing scale. Finally, in Fig. 5(c) we show the energy spectra for two simulations with the same Reynolds number and aspect ratio, but that are forced at different wave numbers. One simulation is forced at $k_f = 20$ and has $\mathrm{Ro} = 0.5$, while the other is forced at $k_f = 30$ and has $\mathrm{Ro} = 0.43$. The evolution of their integral scales is shown in the inset, where the two curves overlap. As in the other two examples, the flux-loop state is sustained when perturbing the system. In this case, making the forcing scale smaller is akin to making the system larger.

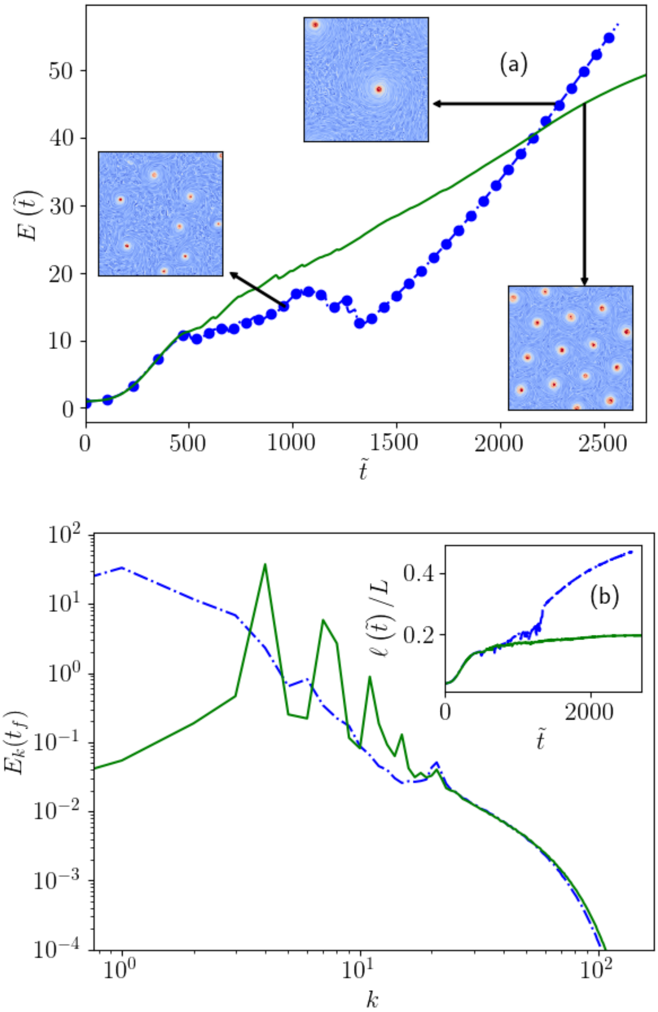

FIG. 4. Results from two simulations with the same parameters, (1,0.45), but that started from different initial conditions. (a): Evolution of the total energy. The solid green line indicates the simulation that stays in the flux-loop regime. The blue line with round symbols indicate the simulation that showed a brief flux loop but then changes to a dual cascade. The insets show visualizations of the parallel component of the vorticity field. (b) Energy spectra for the two simulations, with the same labels as (a). The inset shows the evolution of the integral scale for each simulation.

IV. CONCLUSIONS

By using huge high-performance-computing resources we have studied the (λ, Ro) phase space of rotating turbulence up to a resolution of $512 \times 512 \times 32768$ grid points. We found the existence of a metastable flux-loop regime, where the inverse energy cascade is stopped by a delicate balance between hetero- and homochiral triadic nonlinear interactions, leading to metastable vortex-crystal-like states. These states are stable for very long times but can transition to the inverse cascade regime if perturbed strongly enough.

Observations of multiple large-scale, self-organized turbulent states are becoming more and more common in the turbulent literature, having been observed in bounded flows [43], in anisotropic sheared turbulence [44], in swirling flows [45], and in magnetohydrodamic flows [46]. They play a

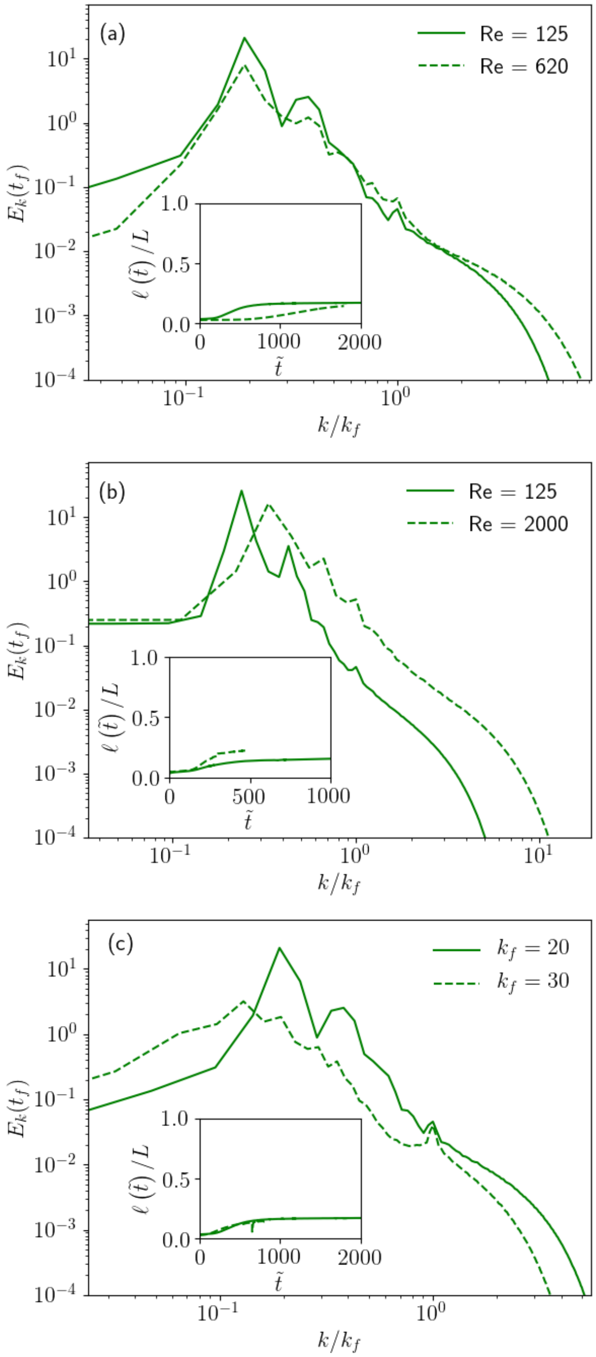

FIG. 5. (a) Energy spectra for two simulations with parameters (1,0.5) but different resolution. The simulation with Re $= 125$ was performed on a grid of 512^3 points, while the simulation with Re $= 2000$ was performed on a grid of 1024^3 points. (b) Energy spectra for two simulations with (16,0.25) but forced at a different wave number. The simulation with Re $= 125$ was forced at $k_f = 20$, while the simulation with Re $= 620$ was forced at $k_f = 8$. (c) Energy spectra for two simulations with Re $= 125$ and $\lambda = 1$. One was forced at $k_f = 20$ and has Ro $= 0.5$, while the other was was forced at $k_f = 30$ and has Ro $= 0.43$. The insets of all three figures show the evolution of the respective integral scales of each simulation.

key role for both fundamental aspects, suggesting the existence of multiple attractors in the system and applied ones, leading to huge variations in the global energetic balance for tiny changes in the control parameters. The present study relates these metastable states with the boundaries of two different states (forward and split cascading) in a phase diagram making the connection with classical phase transitions.

Several important issues remain open, such as the functional behavior of the critical lines that separate the different phases, the robustness of the metastable states in the limit $\mathrm{Ro} \to 0$, $\lambda \to \infty$, and $\lambda \to 0$ [see dashed red lines in the phase-space summary of Fig. 1(a)], and the distribution of the exit times from the crystal state. Furthermore, although the results shown here were found to be robust and stable with respect to changes in the Reynolds number and box size (see Fig. 5), further investigations reaching larger Re and larger box sizes would be desirable.

ACKNOWLEDGMENTS

The authors acknowledge partial funding from the European Research Council under the European Community's Seventh Framework Program, ERC Grant Agreement No. 339032. The simulations have been done using resources provided through the PRACE initiative Pra17_4374 at CINECA. The authors acknowledge P. Mininni and G. Eyink for useful discussions.

APPENDIX A: HELICAL DECOMPOSITION

In this Appendix we provide the definition of the helical fluxes calculated in Figs. 2(a)– 2(c). For this purpose we exploit the decomposition of any incompressible 3D flow into helical modes proposed in Refs. [37,47]. From the incompressibility assumption it follows that $\boldsymbol{u}(\boldsymbol{x})$ is a solenoidal vector field, hence its Fourier modes $\hat{\boldsymbol{u}}(\boldsymbol{k})$ depend only on two linearly independent degrees of freedom, and we can decompose the velocity field as

$$\hat{\boldsymbol{u}}_{\boldsymbol{k}}(t) = \hat{\boldsymbol{u}}_{\boldsymbol{k}}^{+}(t) + \hat{\boldsymbol{u}}_{\boldsymbol{k}}^{-}(t) = \hat{u}_{\boldsymbol{k}}^{+}(t)\mathbf{h}_{+}(\boldsymbol{k}) + \hat{u}_{\boldsymbol{k}}^{-}(t)\mathbf{h}_{-}(\boldsymbol{k}), \tag{A1}$$

where $\mathbf{h}_{\pm}(\boldsymbol{k})$ are the orthogonal eigenmodes of the curl operator, and hence each Fourier mode of the velocity field satisfies

$$i\boldsymbol{k} \times \hat{\boldsymbol{u}}_{\boldsymbol{k}}^{s_k} = s_{\boldsymbol{k}} \hat{\boldsymbol{u}}_{\boldsymbol{k}}^{s_k}, \tag{A2}$$

with $s_{\boldsymbol{k}} = \pm$. The homochiral energy fluxes are made out of triads with the same chirality:

$$\Pi_k^{\mathrm{hom}} = \Pi_k^{(+,+,+)} + \Pi_k^{(-,-,-)}, \tag{A3}$$

$$\Pi_k^{(\pm,\pm,\pm)} = -i \sum_{|\boldsymbol{k}|\leqslant k} \sum_{\boldsymbol{p}+\boldsymbol{q}=\boldsymbol{k}} \left(\hat{\boldsymbol{u}}_{-\boldsymbol{k}}^{\pm} \cdot \hat{\boldsymbol{u}}_{\boldsymbol{p}}^{\pm}\right)\left(\boldsymbol{k} \cdot \hat{\boldsymbol{u}}_{\boldsymbol{q}}^{\pm}\right), \tag{A4}$$

while the heterochiral is given by all resulting triads with two Fourier modes of opposite chirality:

$$\Pi_k^{\mathrm{het}} = \Pi_k - \Pi_k^{\mathrm{hom}}, \tag{A5}$$

where Π_k is the total energy flux defined in the main text as

$$\Pi_k = -i \sum_{|\boldsymbol{k}|\leqslant k} \sum_{\boldsymbol{p}+\boldsymbol{q}=\boldsymbol{k}} (\hat{\boldsymbol{u}}_{-\boldsymbol{k}} \cdot \hat{\boldsymbol{u}}_{\boldsymbol{p}})(\boldsymbol{k} \cdot \hat{\boldsymbol{u}}_{\boldsymbol{q}}). \tag{A6}$$

APPENDIX B: VIDEO MATERIAL

A visualization of the evolution of the inverse and flux-loop cascades can be found in the uploaded video [27]. The movie provided shows the evolution of the inverse and flux-loop cascades. The movie consists of volume renderings of the vorticity component along the direction of rotation, $\boldsymbol{\omega}_z$, as a function of time for three different simulations obtained with (Ro, λ): (0.25,1) split cascade (left panel);,(0.51,1) split/flux loop (center panel), and (0.58,1) flux loop (right panel). Notice the metastable regime shown in the center panel where the inverse cascade first stops in a quasivortex crystal state and then suddenly restarts, due to 3D vortex merging. In the bottom row of the same video we present the energy spectra and total energy evolution for the same three simulations. Notice that while energy increases in both the split-cascade and the flux-loop regimes, the rate of change of the energy is considerably different between the two.

[1] N. Goldenfeld, *Lectures on Phase Transitions and the Renormalization Group* (CRC Press, Boca Raton, FL, 2018).

[2] A. Bovier and F. Den Hollander, *Metastability: A Potential-Theoretic Approach*, A Series of Comprehensive Studies in Mathematics Vol. 351 (Springer, 2016).

[3] J. D. Gunton and M. Droz, *Introduction to the Theory of Metastable and Unstable States*, Lecture Notes in Physics Vol. 183 (Springer, Berlin, 1983).

[4] R. Zwanzig, *Nonequilibrium Statistical Mechanics* (Oxford University Press, Oxford, 2001).

[5] L. Berthier and G. Biroli, Theoretical perspective on the glass transition and amorphous materials, Rev. Mod. Phys. **83**, 587 (2011).

[6] M. C. Marchetti, J. F. Joanny, S. Ramaswamy, T. B. Liverpool, J. Prost, M. Rao, and R. A. Simha, Hydrodynamics of soft active matter, Rev. Mod. Phys. **85**, 1143 (2013).

[7] A. Alexakis and L. Biferale, Cascades and transitions in turbulent flows, Phys. Rep. **767**, 1 (2018).

[8] I. S. Aranson and L. S. Tsimring, Patterns and collective behavior in granular media: Theoretical concepts, Rev. Mod. Phys. **78**, 641 (2006).

[9] G. Lemoult, L. Shi, K. Avila, S. V. Jalikop, M. Avila, and B. Hof, Directed percolation phase transition to sustained turbulence in Couette flow, Nat. Phys. **12**, 254 (2016).

[10] M. Chantry, L. S. Tuckerman, and D. Barkley, Universal continuous transition to turbulence in a planar shear flow, J. Fluid Mech. **824**, R1 (2017).

[11] D. Moxey and D. Barkley, Distinct large-scale turbulent-laminar states in transitional pipe flow, Proc. Natl. Acad. Sci. USA **107**, 8091 (2010).

[12] P. A. Davidson, *Turbulence in Rotating, Stratified and Electrically Conducting Fluids* (Cambridge University Press, Cambridge, 2013).

[13] A. Campagne, B. Gallet, F. Moisy, and P.-P. Cortet, Direct and inverse energy cascades in a forced rotating turbulence experiment, Phys. Fluids **26**, 125112 (2014).

[14] A. Pouquet and R. Marino, Geophysical Turbulence and the Duality of the Energy Flow Across Scales, Phys. Rev. Lett. **111**, 234501 (2013).

[15] E. Yarom and E. Sharon, Experimental observation of steady inertial wave turbulence in deep rotating flows, Nat. Phys. **10**, 510 (2014).

[16] P. Sagaut and C. Cambon, *Homogeneous Turbulence Dynamics* (Springer, 2008).

[17] L. M. Smith and F. Waleffe, Transfer of energy to two-dimensional large scales in forced, rotating three-dimensional turbulence, Phys. Fluids **11**, 1608 (1999).

[18] E. Deusebio, G. Boffetta, E. Lindborg, and S. Musacchio, Dimensional transition in rotating turbulence, Phys. Rev. E **90**, 023005 (2014).

[19] T. Pestana and S. Hickel, Regime transition in the energy cascade of rotating turbulence, Phys. Rev. E **99**, 053103 (2019).

[20] T. Pestana and S. Hickel, Rossby-number effects on columnar eddy formation and the energy dissipation law in homogeneous rotating turbulence, J. Fluid Mech. **885**, A27 (2020).

[21] S. Galtier, Weak inertial-wave turbulence theory, Phys. Rev. E **68**, 015301(R) (2003).

[22] A. van Kan and A. Alexakis, Critical transition in fast-rotating turbulence within highly elongated domains, J. Fluid Mech. **899**, A33 (2020).

[23] H. Aref, P. K. Newton, M. A. Stremler, T. Tokieda, and D. L. Vainchtein, *Vortex crystals* (Department of Theoretical and Applied Mechanics (UIUC), 2002).

[24] G. Falkovich, Bottleneck phenomenon in developed turbulence, Phys. Fluids **6**, 1411 (1994).

[25] L. Biferale, F. Bonaccorso, I. M. Mazzitelli, M. A. T. van Hinsberg, A. S. Lanotte, S. Musacchio, P. Perlekar, and F. Toschi, Coherent Structures and Extreme Events in Rotating Multiphase Turbulent Flows, Phys. Rev. X **6**, 041036 (2016).

[26] F. Waleffe, Inertial transfers in the helical decomposition, Phys. Fluids A **5**, 677 (1993).

[27] See Supplemental Material at http://link.aps.org/supplemental/10.1103/PhysRevFluids.5.104603 for the video described in Appendix B.

[28] H. Aref and D. L. Vainchtein, Point vortices exhibit asymmetric equilibria, Nature (London) **392**, 769 (1998).

[29] K. S. Fine, A. C. Cass, W. G. Flynn, and C. F. Driscoll, Relaxation of 2D Turbulence to Vortex Crystals, Phys. Rev. Lett. **75**, 3277 (1995).

[30] X.-P. Huang and C. F. Driscoll, Relaxation of 2D Turbulence to a Metaequilibrium Near the Minimum Enstrophy State, Phys. Rev. Lett. **72**, 2187 (1994).

[31] J. Jiménez and A. Guegan, Spontaneous generation of vortex crystals from forced two-dimensional homogeneous turbulence, Phys. Fluids **19**, 085103 (2007).

[32] J. R. Abo-Shaeer, C. Raman, J. M. Vogels, and W. Ketterle, Observation of vortex lattices in Bose-Einstein condensates, Science **292**, 476 (2001).

[33] P. K. Newton and G. Chamoun, Vortex lattice theory: A particle interaction perspective, SIAM Rev. **51**, 501 (2009).

[34] A. Adriani, A. Mura, G. Orton, C. Hansen, F. Altieri, M. L. Moriconi, J. Rogers, G. Eichstädt, T. Momary, A. P. Ingersoll *et al.*, Clusters of cyclones encircling Jupiter's poles, Nature (London) **555**, 216 (2018).

[35] V. Dallas, S. Fauve, and A. Alexakis, Statistical Equilibria of Large Scales in Dissipative Hydrodynamic Turbulence, Phys. Rev. Lett. **115**, 204501 (2015).

[36] A. Alexakis and M.-E. Brachet, On the thermal equilibrium state of large-scale flows, J. Fluid Mech. **872**, 594 (2019).

[37] F. Waleffe, The nature of triad interactions in homogeneous turbulence, Phys. Fluids A **4**, 350 (1992).

[38] A. Alexakis, Helically decomposed turbulence, J. Fluid Mech. **812**, 752 (2017).

[39] G. Sahoo and L. Biferale, Energy cascade and intermittency in helically decomposed Navier–Stokes equations, Fluid Dyn. Res. **50**, 011420 (2018).

[40] L. Biferale, M. Buzzicotti, and M. Linkmann, From two-dimensional to three-dimensional turbulence through two-dimensional three-component flows, Phys. Fluids **29**, 111101 (2017).

[41] M. Buzzicotti, H. Aluie, L. Biferale, and M. Linkmann, Energy transfer in turbulence under rotation, Phys. Rev. Fluids **3**, 034802 (2018).

[42] M. Buzzicotti, P. C. Di Leoni, and L. Biferale, On the inverse energy transfer in rotating turbulence, Eur. Phys. J. E **41**, 131 (2018).

[43] S. G. Huisman, R. C. A. van der Veen, C. Sun, and D. Lohse, Multiple states in highly turbulent Taylor–Couette flow, Nat. Commun. **5**, 3820 (2014).

[44] K. P. Iyer, F. Bonaccorso, L. Biferale, and F. Toschi, Multiscale anisotropic fluctuations in sheared turbulence with multiple states, Phys. Rev. Fluids **2**, 052602 (2017).

[45] D. Faranda, Y. Sato, B. Saint-Michel, C. Wiertel, V. Padilla, B. Dubrulle, and F. Daviaud, Stochastic Chaos in a Turbulent Swirling Flow, Phys. Rev. Lett. **119**, 014502 (2017).

[46] J. V. Shebalin, Broken ergodicity in two-dimensional homogeneous magnetohydrodynamic turbulence, Phys. Plasmas **17**, 092303 (2010).

[47] P. Constantin and A. Majda, The Beltrami spectrum for incompressible fluid flows, Commun. Math. Phys. **115**, 435 (1988).